Journal of Nanobiotechnology

RESEARCH Open Access

Apoptotic body based biomimetic hybrid nanovesicles to attenuate cytokine storms for sepsis treatment

Hongbing Lan[1,2†], Zhanhao Zhou[3†], Qian Hu[2], Qi Xie[2], Xiaonan Li[2], Tianyi Tian[2], Yi Wang[2], Conglian Yang[2], Li Kong[2], Dehao Fu[4*], Yuanyuan Guo[3,5*] and Zhiping Zhang[2,6*]

Abstract

Sepsis is a severe immune response to pathogens that is associated with high mortality rate and a paucity of efficacious treatment options. It is characterized by the hyperactivation of macrophages and the occurrence of cytokine storms. Given the anti-inflammatory properties of M2 macrophages and their derived apoptotic bodies (AB), as well as the specific uptake of these by macrophages, a novel approach was employed to combine AB with artificial liposomes to create apoptotic body based biomimetic hybrid nanovesicles (L-AB). The L-AB effectively inherited "eat me" signaling molecules on the surface of the AB, thereby facilitating their targeted uptake by macrophages in both in vitro and in vivo settings. The administration of L-AB for the delivery of dexamethasone effectively augmented the therapeutic efficacy of the drug, mitigated macrophage hyperactivation and tissue damage in vivo, and consequently enhanced the survival rate of septic mice. Taken together, these findings suggest that the apoptotic body biomimetic nanovesicles may represent a potential drug delivery system capable of specifically targeting macrophages for the treatment of sepsis.

Keywords Sepsis, Macrophages, Cytokine storm, Apoptotic body, Biomimetic carrier

Introduction

Sepsis is a complex and lethal disease that affects a significant number of people worldwide each year, with an estimated mortality rate of approximately 50% [1]. Sepsis frequently arises from the infection induced immune dysregulation, which can result in tissue injury and subsequent progression to multiple organ dysfunction syndrome (MODS) [2]. Throughout the pathogenesis of sepsis, hyperactivated macrophages release a plethora of inflammatory mediators, such as interleukin-6 (IL-6), tumor necrosis factor-α (TNF-α), and monocyte chemotactic protein 1 (MCP-1) [3]. The substantial secretion of pro-inflammatory mediators and infiltration of immune cells result in tissue injury. Macrophages play a pivotal role in the initiation and progression of septic inflammation. Targeting macrophage to inhibit their

†Hongbing Lan and Zhanhao Zhou contributed equally to this work.

*Correspondence:
Dehao Fu
fudehao@sjtu.edu.cn
Yuanyuan Guo
yuanyuanguo@hust.edu.cn
Zhiping Zhang
zhipingzhang@mail.hust.edu.cn
[1]Department of Pharmacy, Nanxishan Hospital of Guangxi Zhuang Autonomous Region, Guilin 541002, China
[2]Tongji School of Pharmacy, Huazhong University of Science and Technology, Wuhan 430030, China
[3]Liyuan Hospital, Tongji Medical College, Huazhong University of Science and Technology, Wuhan 430030, China
[4]Department of Orthopaedics, Shanghai Jiaotong University Affiliated Shanghai Sixth People's Hospital, Shanghai 200025, China
[5]Hubei Key Laboratory of Metabolic Abnormalities and Vascular Aging, Huazhong University of Science and Technology, Wuhan 430077, China
[6]National Engineering Research Center for Nanomedicine, Huazhong University of Science and Technology, Wuhan 430030, China

overactivation may represent a promising avenue for therapeutic approach in sepsis [4, 5].

Extracellular vesicles (EV) serve as carriers for signaling molecules in intercellular communication and can transport a range of functional molecules, including proteins, nucleic acids, and lipids, to enable their biological functions [6]. EV possess distinctive advantages, such as reduced immunogenicity, specific targeting capabilities, prolonged circulation time, and the capacity to traverse biological barriers, rendering them compelling candidates for drug delivery vehicles [7, 8]. Apoptotic bodies (AB) constitute a subset of EV, characterized by the presence of a complete outer membrane. This membrane is generated through the blistering and protrusion of apoptotic membranes during the disintegration of apoptotic cells [9, 10]. In contrast to exosomes and microvesicles, which are internalized by cells through phagocytosis and endocytosis [11], AB possess the ability to transmit "find me" and "eat me" signals that attract phagocytic cells for phagocytosis [12, 13]. In addition, AB can serve crucial functions in intercellular communication, immune modulation, procoagulant activity, and the maintenance of physiological homeostasis [14–16]. The presence of phosphatidylserine (PS) on the surface of AB enables its recognition and subsequent elimination by macrophages, thereby initiating anti-inflammatory and immunoregulatory effects [17, 18]. Consequently, AB may be utilized as an effective carrier for targeting macrophages.

In order to enhance the loading efficiency of drug delivery systems, a range of techniques have been developed to load drugs into AB, including passive loading, active loading, and the construction of biomimetic carriers through the encapsulation of AB with nanovesicles [19]. Passive loading involves the introduction of nucleic acids and proteins into AB or the treatment of cells with drug-loaded nanoparticles, which might induce cell apoptosis and facilitate the incorporation of drug-loaded nanoparticles into AB [20]. Active loading methods for drugs into AB include electroporation, sonication, and saponin-mediated decontamination permeabilization, freeze-thaw cycling, and extrusion [21]. The aforementioned methods are constrained by their complexity and inefficiency. The biomimetic carriers based on natural apoptotic body membranes coated nanoparticles have been identified as a promising approach for improving drug delivery efficacy [22–24]. However, this approach may potentially result in the loss of bioactive components of AB. Hence, it is essential to further explore methods that can improve drug loading efficiency while preserving the bioactive components of AB.

Our previous researches have shown that hybrid nanovesicles, which are constructed by fusing liposomes with cell-extruded nanovesicles, exhibit high drug encapsulation efficiency, retain biological function and enhance targeting capabilities [25–27]. It can therefore be proposed that the development of apoptotic body biomimetic nanovesicles using the hybrid approach may prove an effective strategy for targeted drug delivery. Furthermore, the potential of M2 macrophages-derived EV (M2-EV) in the treatment of inflammatory diseases has attracted considerable interest [28]. It has been demonstrated that M2-EV are capable of suppressing key inflammatory signaling pathways, attenuating endotoxin-induced cytokine storms, and mitigating organ damage [29]. Moreover, M2-EV have been found to impede the migration of polymorphonuclear leukocytes and the formation of neutrophil extracellular traps, thereby reducing mortality rates in septic mice [30]. Consequently, it is postulated that M2 macrophage-derived AB may act as regulators of the inflammatory response in sepsis.

In this study, AB-based biomimetic hybrid nanovesicles (L-AB) were prepared by fusing liposomes with AB derived from M2 macrophages (Scheme 1). Dexamethasone (Dex), a glucocorticoid with potent anti-inflammatory properties, has been shown to suppress immune cell over-activation and cytokine storms, making it a common option for acute respiratory distress syndrome (ARDS) and sepsis [31, 32]. Dex-loaded L-AB (Dex@L-AB) retained the "eat me" signal of apoptotic bodies, which could effectively deliver Dex to macrophages. After tail vein administration, Dex@L-AB was rapidly distributed to the major organs of septic mice, where it was internalized by macrophages, effectively inhibiting macrophage overactivation and alleviating the cytokine storm induced tissue damage, leading to improved survival rates compared to free Dex. In conclusion, the construction of biomimetic nanovesicles based on AB may represent an efficient approach for targeted drug delivery to macrophages and potent anti-inflammatory treatment of sepsis.

Results and discussion

Preparation and characterization of L-AB

Following the induction of IL-4, M2-type macrophages exhibited high levels of CD206 expression (Fig. S1). These macrophages were subsequently induced for the isolation of AB. The AB were combined with liposomes to fabricate L-AB. A lipid film was prepared using DOPC, cholesterol, and DSPE-PEG2000 at a molar ratio of 8:8:1 by the solvent evaporation method. Subsequently, the AB suspension was hydrated with the prepared lipid film and extruded through the polycarbonate membranes to produce L-AB. The morphological features of AB, LIP and L-AB were observed using transmission electronic microscopy (TEM). As displayed in Fig. 1A, the AB exhibited a larger spherical vesicle structure with a particle size of approximately 1000 nm, in contrast to LIP and L-AB, which had significantly smaller particle sizes of

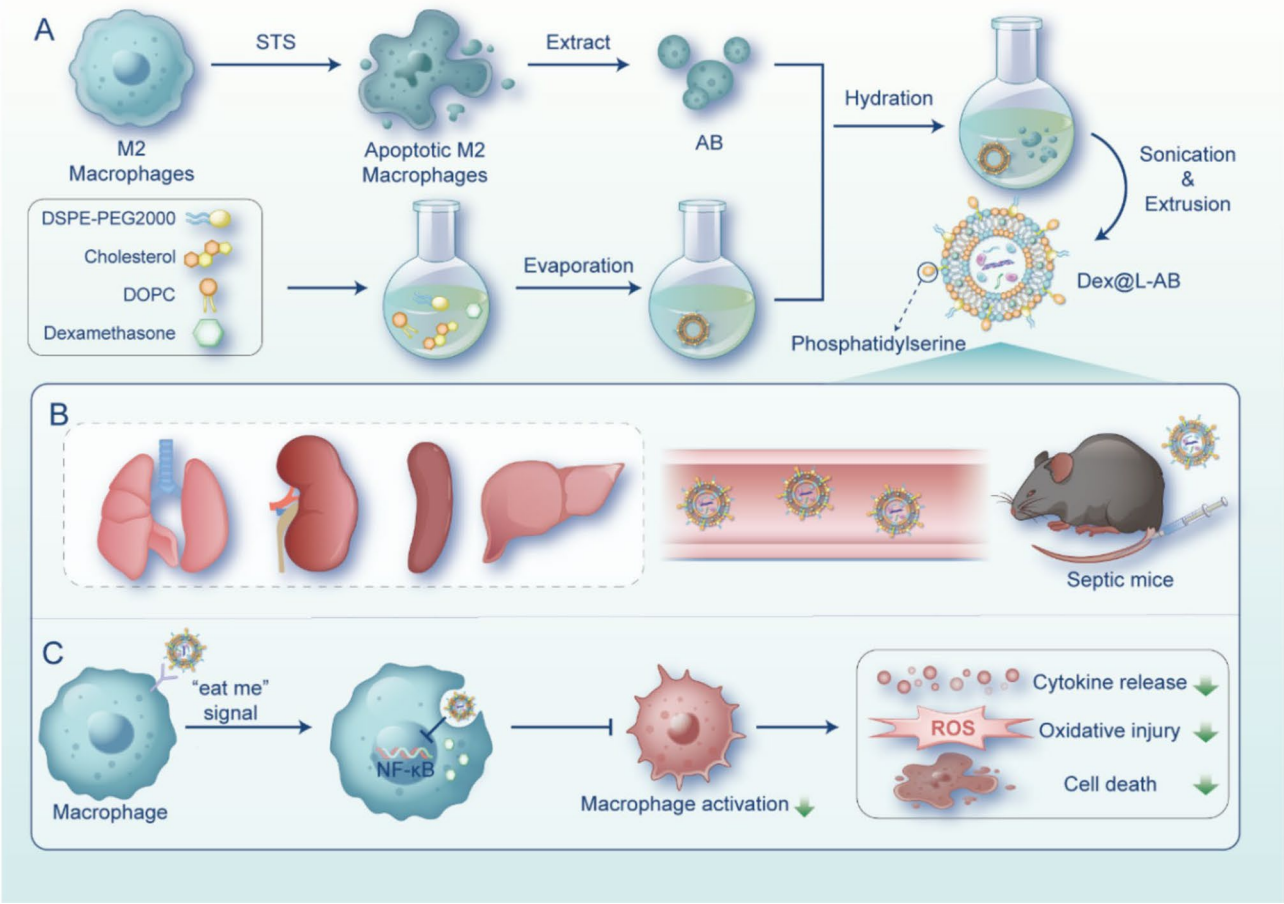

Scheme 1 Schematic illustration of apoptotic body based biomimetic hybrid nanovesicles for sepsis therapy. **(A)** Scheme of Dex@L-AB preparation process. (**B**) Dex@L-AB distributed to the major organs of septic mice through blood circulation after intravenous injection. (**C**) Upon recognition by macrophages through the "eat me" signal, Dex@L-AB is internalized and released into the cells to inhibit NF- κB pathway, thereby suppressing macrophage activation and reducing cytokine release, oxidative damage, and cell death. Painted by FigDraw

approximately 200 nm and also showed a similar spherical vesicle structure. Subsequently, the particle size, polydispersity index (PDI), and ζ potential of the nanovesicles were determined by dynamic light scattering (DLS), and the results were presented in Fig. 1B. In accordance with TEM results, L-AB exhibited a diameter of approximately 151.07±2.96 nm (PDI, 0.222±0.025), whereas the LIP and AB displayed diameters of 169.27±2.48 nm (PDI, 0.215±0.023) and 984.84±13.87 nm (PDI, 0.383±0.047), respectively. Besides, the decreased PDI indicated that L-AB possessed superior size homogeneity in comparison AB. The ζ potential of L-AB was observed to be -5.05±2.20 mV, which was decreased compared to LIP (-0.15±3.08mV). This discrepancy is likely due to the insertion of AB membrane proteins (-9.95±2.70 mV). The colloidal stability of LIP, AB and L-AB was subsequently evaluated by monitoring the particle size over a period of 7 days. Both LIP and L-AB demonstrated stability over a period of one week in biologically relevant solutions, as indicated by minimal changes in particle size. In contrast, the particle size of AB decreased from 984 to 531 nm over the subsequent day (Fig. S2). These results indicated that the fusion of AB with the synthetic liposomes favored the structural stability of AB. The findings indicated that the fusion of AB with synthetic liposomes resulted in improved structural stability of AB.

To investigate the co-fusion of LIP and AB, LIP and AB were labeled with red (DiI) and green (DiO) fluorescent dyes, respectively, and imaged using a confocal laser scanning microscope (CLSM) to validate the efficiency of co-fusion. As shown in Fig. 1C, the physically mixed DiI@LIP and DiO@AB exhibited a segregated distribution. Following the execution of the hydration and coextrusion, the red (DiI) and green (DiO) fluorescence signals in L-AB exhibited substantial overlapped. The merged fluorescence images revealed a significant degree of co-localization between the fluorescence signals of LIP and AB, suggesting that effective fusion between LIP and AB. Similarly, Förster resonance energy transfer (FRET) was also employed to confirm the fusion of LIP and AB, utilizing DiI (a fluorescent donor) and DiD (a fluorescent acceptor). DiI and DiD co-labeled AB were fused

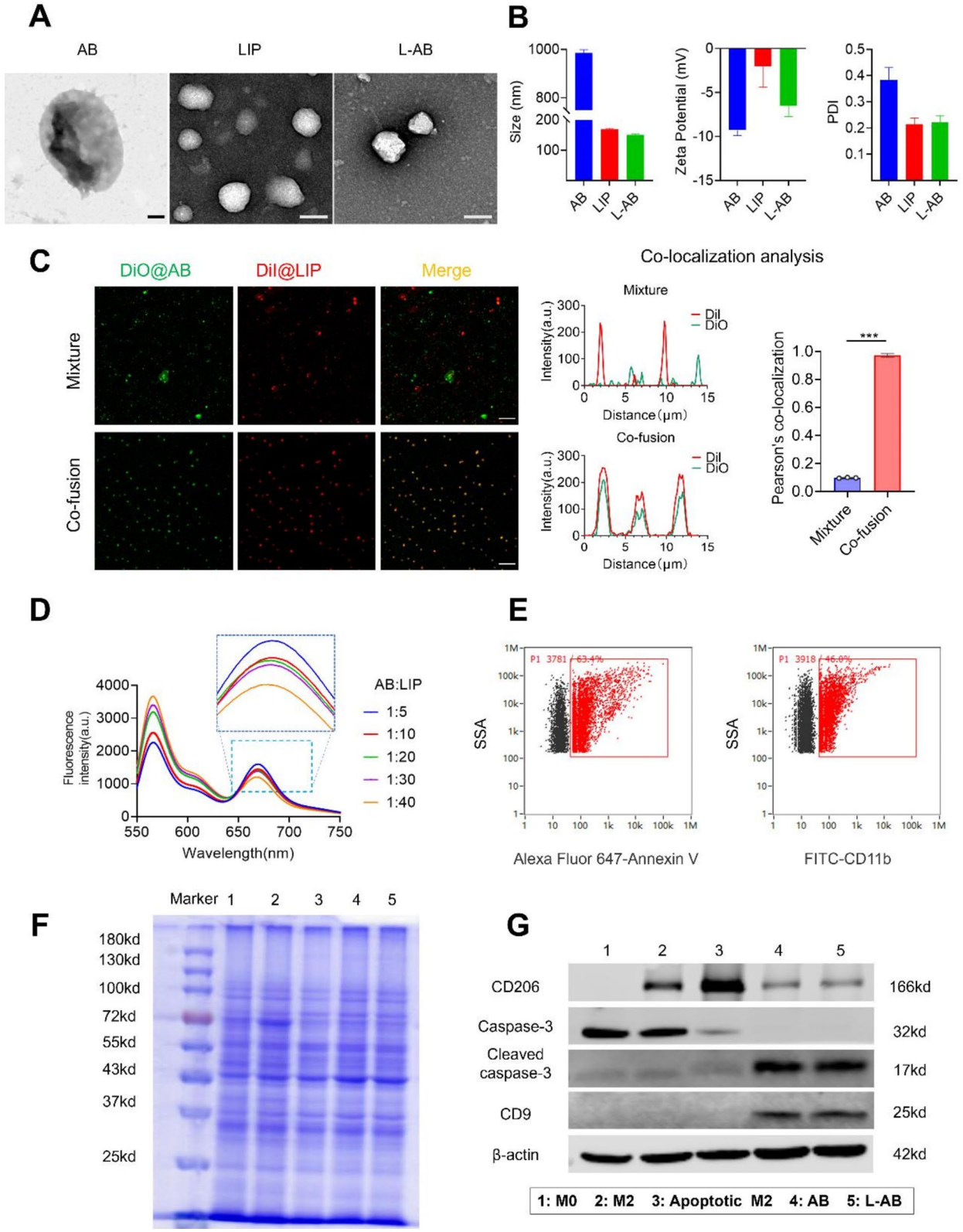

Fig. 1 Preparation and characterization of L-AB. (**A**) TEM images of AB, LIP and L-AB. Scale bar = 200 nm. (**B**) Hydrodynamic size distribution and ζ potential of AB, LIP, and L-AB ($n = 3$). (**C**) CLSM images and co-localization analysis of a physical mixture (LIP with AB) (mixture) and L-AB (co-fusion) (red, LIP-DiI; green, AB-DiO; Scale bar = 10 μm). (**D**) FRET results of L-AB with different fusion ratios of LIP and AB. (**E**) The expression of PS and CD11b on the L-AB surface which was detected by nanoflow cytometry. (**F**) SDS-PAGE images of marker, 1: M0; 2: M2; 3: apoptotic M2; 4: AB; 5: L-AB.(**G**) Western blot of specific makers of the M0/M2/apoptotic M2 cell, AB and L-AB, 1: M0; 2: M2; 3: apoptotic M2; 4: AB; 5: L-AB

with blank LIP in different ratios. As shown in Fig. 1D, an increase in the quantity of LIP was accompanied by an enhancement in fluorescence at 565 nm, while a decline was observed at 670 nm. These results indicated that the LIP and AB can be fused to form hybrid nanovesicles. Furthermore, the surface of AB exhibited a considerable abundance of PS, a molecule renowned for its robust binding affinity to Annexin V, as illustrated in Fig. S3. To ascertain the prevalence of PS and CD11b (a macrophage surface protein) on the surface of L-AB, nanoflow cytometry was employed in the investigation. The results revealed a high expression of PS (63.4%) and CD11b (46.0%) on L-ABs, as depicted in Fig. 1E. The results demonstrated that L-AB inherited some of the bioactive components such as PS from AB, which makes it likely to have similar biological functions as AB.

Subsequently analysis of AB and L-AB was conducted by sodium dodecyl sulfate-polyacrylamide gel electrophoresis (SDS-PAGE) to assess the efficacy of protein preservation. As shown in Fig. 1F, the protein profiles of the M2 macrophages exhibited similarities to those of the original M0 cells with minor variations. The protein profiles of AB and L-AB were analogous to the total protein band of M2 cells that they were derived from, indicating superior protein retention. Moreover, the retention of key proteins on L-AB was further corroborated by Western blot (Fig. 1G). The expression of CD206 in M2 macrophages was found to be significantly elevated in comparison to that observed in M0 macrophages, thereby confirming the successful induction of M2 macrophages. The analysis of AB revealed the presence of the CD206 protein, derived from M2 macrophages, alongside an increased expression of the extracellular vesicle marker CD9. Additionally, elevated levels of cleaved caspase-3 (an apoptosis-related marker) were detected. Notably, the aforementioned proteins exhibited comparable levels in L-AB as observed in AB, indicating that L-AB effectively inherits the characteristic proteins of AB. However, the absence of a purification step for L-AB, despite the CLSM data indicating that the majority of AB fused with LIP, may have resulted in a small amount of unfused AB being inadvertently included, which could potentially interfere with the experimental outcomes.

Cellular uptake and anti-inflammatory ability at the cellular level

Firstly, the viability of RAW264.7 cells was examined following the administration of LIP, AB and L-AB, using 3-(4,5-dimethylthiazol-2-yl)-2,5-diphenyltetrazolium bromide (MTT) assay. As indicated in Fig. S4, no obvious cytotoxic effects were observed and L-AB displayed safety on RAW264.7 cells. Subsequently, the uptake characteristics of AB, LIP and L-AB by macrophages were evaluated. A significant red fluorescence signal was observed in the AB and L-AB groups compared to that in the LIP groups (Fig. 2A), indicating that AB and L-AB were taken up by macrophages with high efficiency. This phenomenon might be attributed to the clearance of AB by macrophages. Next, the time-dependent uptake of L-AB by macrophages was examined. As expected, the fluorescence intensity increased with the duration of the incubation period. The mean fluorescence intensity (MFI) of the L-AB group was observed to be greater than that of the LIP group at 1 h, although this difference was not statistically significant. In contrast, the MFI of the L-AB group was higher than that of the LIP group at 3 and 5 h. This disparity might be attributed to the presence of PEG on the surface of the L-AB, which may impede its uptake by macrophages (Fig. 2B-C). The MFI of macrophages ingesting AB was significantly higher than that of LIP and L-AB. This might be attributed to the size of AB, which was significantly larger than that of LIP and L-AB. It has been demonstrated that macrophages phagocytizing larger volumes of nanoparticles under the same conditions ingest more fluorescent dyes. To confirm the targeted uptake of L-AB by macrophages, control recipient cells were selected from AML12 (alpha mouse liver 12), HUEVC (human umbilical vein endothelial cells), L929 (mouse fibroblast), and MLE12 (mouse lung epithelial cells). The findings indicated that macrophages exhibited higher uptake efficiency with L-AB compared to AML12, HEUVC, L929 and MLE12 when subjected to identical conditions (Fig. 2D). This result indicated that L-AB could be specifically taken up by macrophages. Consequently, L-AB may possess the potential to be selectively targeted for uptake by macrophages in vivo.

In addition to PS, calreticulin, Growth arrest-specific 6 (Gas6), protein S, and other proteins also serve as crucial "eat me" signals that enable macrophages to recognize apoptotic cells [33]. MerTK is a prevalent "eat me" signaling receptor that is located on the surface of macrophages [13]. To elucidate the role of PS in the recognition of L-AB by macrophages, annexin V (ANXA5) was employed to block PS on the surface of L-AB, and UNC2250 was utilized to inhibit the expression of the MerTK receptor in macrophages [34]. The results demonstrated a significant reduction in macrophage uptake of L-AB following blockade by ANXA5. Furthermore, the inhibition of MerTK receptor effectively reduced the uptake of L-AB by macrophages (Fig. S5). These findings suggested that, in addition to PS, other "eat me" signals were likely involved in the recognition of L-AB by macrophages.

Furthermore, a range of chemical inhibitors were employed to elucidate the endocytic pathways of L-AB through flow cytometry (FCM) analysis. Specifically, chlorpromazine and sucrose were utilized as inhibitors of clathrin-mediated endocytosis, while

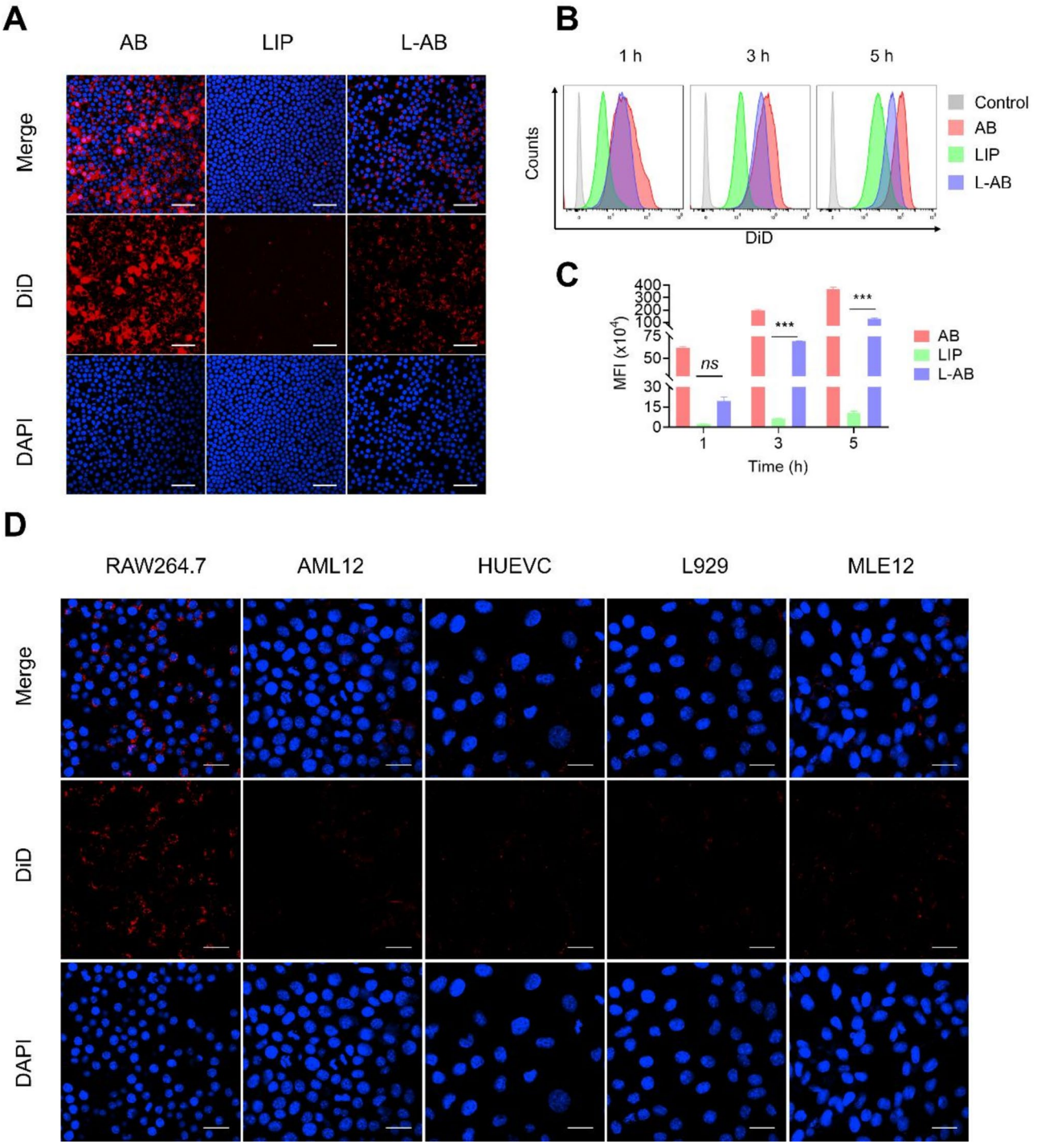

Fig. 2 Cellular uptake of L-AB. (**A**) Fluorescence images of cellular uptake of AB, LIP, and L-AB on RAW264.7. Scale bar = 50 μm. (**B**, **C**) FCM quantification of the in vitro cellular uptake of AB, LIP, and L-AB by RAW264.7 ($n = 3$). (**D**) Cellular uptake of L-AB in different cells. Scale bar = 25 μm. Data are displayed as mean ± SD. ***$P < 0.001$, *ns.*, not significant

methyl-β-cyclodextrin (M-β-CD) and amiloride hydrochloride served as inhibitors of macropinocytosis and lipid raft-mediated endocytosis, respectively [35–37]. As shown in Fig. S6, the uptake of L-AB by macrophages was significantly reduced following treatment with M-β-CD and amiloride, whereas chlorpromazine and sucrose exhibited no discernible impact on the efficacy of L-AB uptake. These observations indicated that macropinocytosis and lipid raft-mediated endocytosis represented the primary mechanism through which L-AB was

internalized by macrophages. Furthermore, the involvement of macropinocytosis in the uptake of L-AB might be mediated by "eat-me" signals presented on the surface of L-AB. Previous studies have demonstrated that "eat-me" signals, including PS, might prompt macrophages to internalize apoptotic cells and apoptotic vesicles via micropinocytosis [38–40].

Dex, a hydrophobic anti-inflammatory agent, was employed as a model molecule for evaluating the efficacy of drug delivery by L-AB. The encapsulation efficiency of Dex within L-AB was conducted using high-performance liquid chromatography (HPLC). The results demonstrated an encapsulation efficiency of 68.66±7.74% for Dex within L-AB (Fig. S7). Furthermore, the encapsulated Dex exhibited a sustained release pattern, with approximately 78.5% of the drug released from the L-AB over a 48 h period (Fig. 3A).

A cytokine storm frequently results in an excessive production of reactive oxygen species (ROS), which might lead to oxidative damage and the amplification of inflammation [41, 42]. The impact of Dex@L-AB on the protection against intracellular endogenous ROS, inducing by lipopolysaccharides (LPS) stimulation, was examined. As shown in Fig. 3B-C, intracellular ROS levels was observed to increase following LPS treatment. In contrast, Dex was observed to downregulate ROS levels in inflammatory macrophages. Furthermore, the ROS level in the Dex@L-AB group was unexpectedly slightly lower than that in the Dex group. This phenomenon may be attributed to the utilization of L-AB as a carrier, which facilitated the increased uptake of Dex by macrophages, thereby augmenting its anti-inflammatory efficacy. Furthermore, comparable anti-inflammatory effects were observed in the measurements of NO levels (Fig. 3D).

The impact of Dex@L-AB on the inhibition of pro-inflammatory cytokines was subsequently investigated by measuring the levels of IL-6, interferon-γ (IFN-γ), and TNF-α (Fig. 3E-G). The cytometric bead array (CBA) analysis revealed a significant increase in cytokine secretion by LPS-stimulated macrophages, with Dex and AB demonstrating varying degrees of inhibitory efficacy. As anticipated, Dex@L-AB was more effective in inhibiting pro-inflammatory factors.

The nuclear translocation of nuclear factor kappa-B (NF-κB) is a pivotal event in the release of inflammatory mediators [43]. Activation of the NF-κB signaling pathway induces the translocation of p65 to the nucleus, where it modulates the transcription of genes associated with inflammation [44]. p65 is predominantly located in the cytosol in unstimulated macrophages (Fig. 3H). However, upon stimulation with LPS, p65 accumulated in the nucleus. Following Dex treatment, p65 nuclear translocation was observed to be reduced, yet a portion of it still entered the nucleus. The results demonstrated that Dex@LIP and Dex@L-AB effectively inhibited p65 nuclear translocation, with Dex@L-AB exhibiting a more pronounced inhibitory effect. The reason for this might be that macrophages might take up more drugs through nanoparticles, and Dex@L-AB have a higher uptake efficiency and thus the best efficacy. In summary, the Dex@L-AB may exert multifarious anti-inflammatory effects by inhibiting the NF-κB signaling pathway, reducing NO, inflammatory cytokines, and scavenging ROS.

Ex vivo biodistribution of L-AB

During the process of apoptosis, PS acts as a key "eat-me" signal, exposing itself on the surface of apoptotic cells and AB [12]. This facilitates the specific recognition by macrophages and subsequent internalization of the corpse [12]. It was thus decided to take advantage of the high affinity of macrophages for PS by constructing L-AB for targeted drug delivery to macrophages. To track the in vivo distribution of AB, LIP, and L-AB, septic or healthy mice were intravenously injected with fluorescently labeled AB, LIP, or L-AB. The in vivo imaging system demonstrated that systemically administered AB were mainly localized in the liver and spleen of septic mice, which are the major organs of the mononuclear phagocyte system. This finding aligns with the observation reported studies [45]. It was demonstrated that nanoparticles injected via the tail vein could accumulate in the lungs of septic mice, likely due to endothelial damage and the resultant hyperpermeability [46]. As a result, the increase in lung permeability led to the accumulation of LIP and L-AB in the lungs. L-AB demonstrated a more effectively accumulation and retention effect in the lungs of septic mice, exhibiting a fluorescence intensity approximately 1.6-fold greater than that of LIP at 4 h ($p<0.001$). In addition, the distribution of L-AB in the liver, spleen, and kidneys was more extensive than that of LIP within the initial four hours (Fig. 4A-B, Fig. S8). This phenomenon might be attributed to the presence of an "eat me" signal on the surface of L-AB.

In the initial 4 h following the onset of sepsis, the distribution of L-AB in the liver, spleen, and kidneys of septic mice was found to be higher than that observed in healthy mice. The distribution of L-AB in the liver, spleen, and kidneys of healthy mice was found to be higher than that of septic mice at 12 h. This phenomenon might be attributed to the accumulation of immune cells, including macrophages, in the aforementioned organs, which facilitates the accelerated distribution of L-AB in inflammatory organs. Conversely, L-AB was distributed and metabolized at a relatively slow rate in healthy mice that did not have an overactivated immune system in vivo. Furthermore, it was observed that the brightness of certain tissues increased after 4 h compared to 1 h. However, the mean fluorescence signal of tissues at 4 h was found

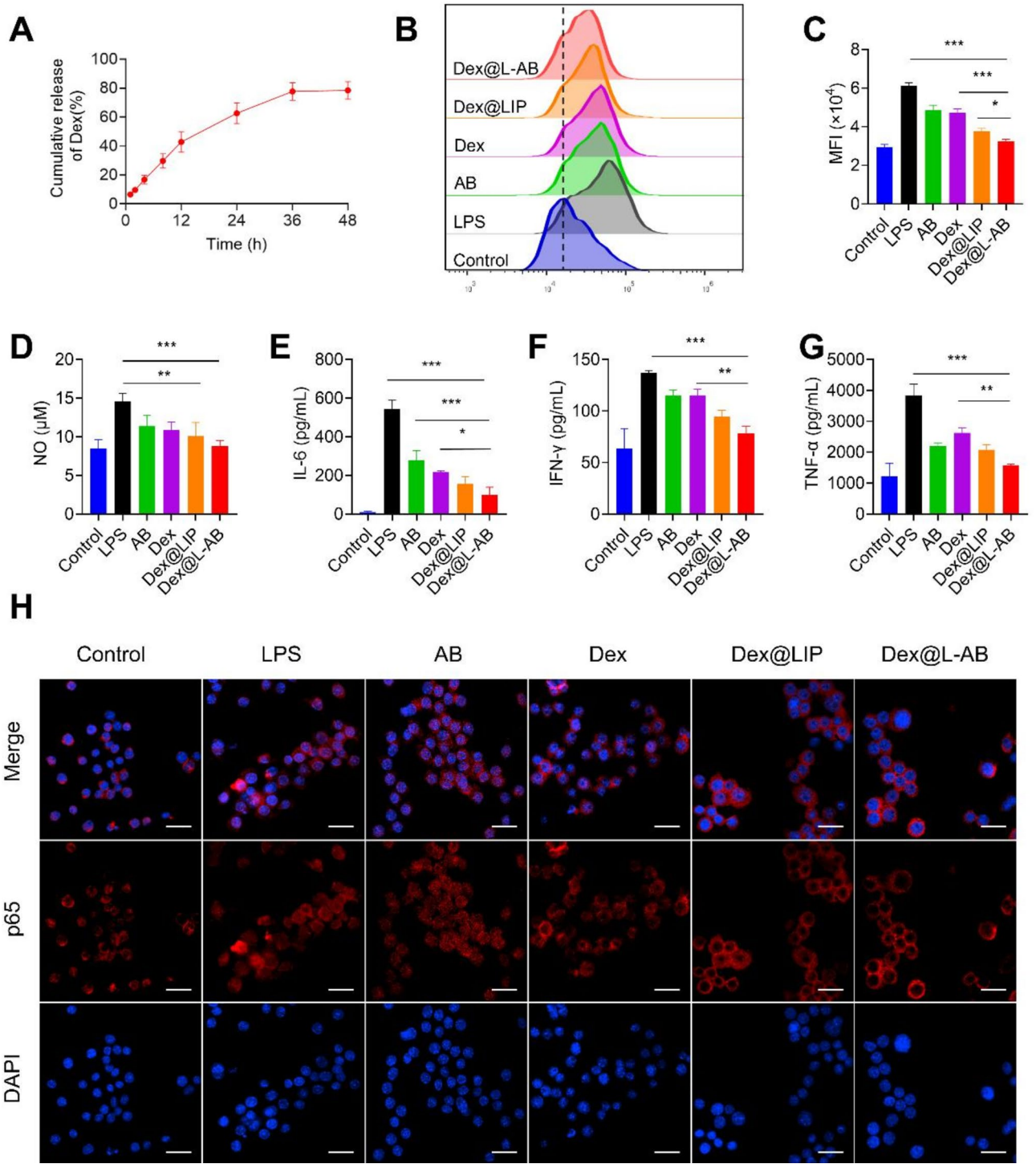

Fig. 3 In vitro anti-inflammatory and antioxidant activities of Dex@L-AB. (**A**) Release profiles of Dex@L-AB ($n = 3$). (**B**, **C**) Quantitative detection and analysis of intracellular ROS levels by FCM on RAW264.7 ($n = 3$). (**D**) NO from the supernatant of inflamed macrophages after incubation with various treatments ($n = 3$). (**E-G**) Cytokine levels of IL-6, IFN-γ, and TNF-α from the supernatant of inflamed macrophages after incubation with various treatments ($n = 3$). (**H**) Detection of p65 nuclear translocation via immune-fluorescence staining, scale bar = 25 μm. Data are displayed as mean ± SD. $^{**}P < 0.01$, $^{***}P < 0.001$

to be lower than at 1 h. One potential explanation for this phenomenon was that as inflammation progresses, there was a rise in the presence of inflammatory cells and tissue swelling, resulting in an increase in tissue mass (Fig. S9).

Furthermore, an analysis was conducted on the fluorescence intensity in blood, which revealed that the distribution of AB was lower compared to that of LIP and L-AB (Fig. S10). This disparity might be attributed to the

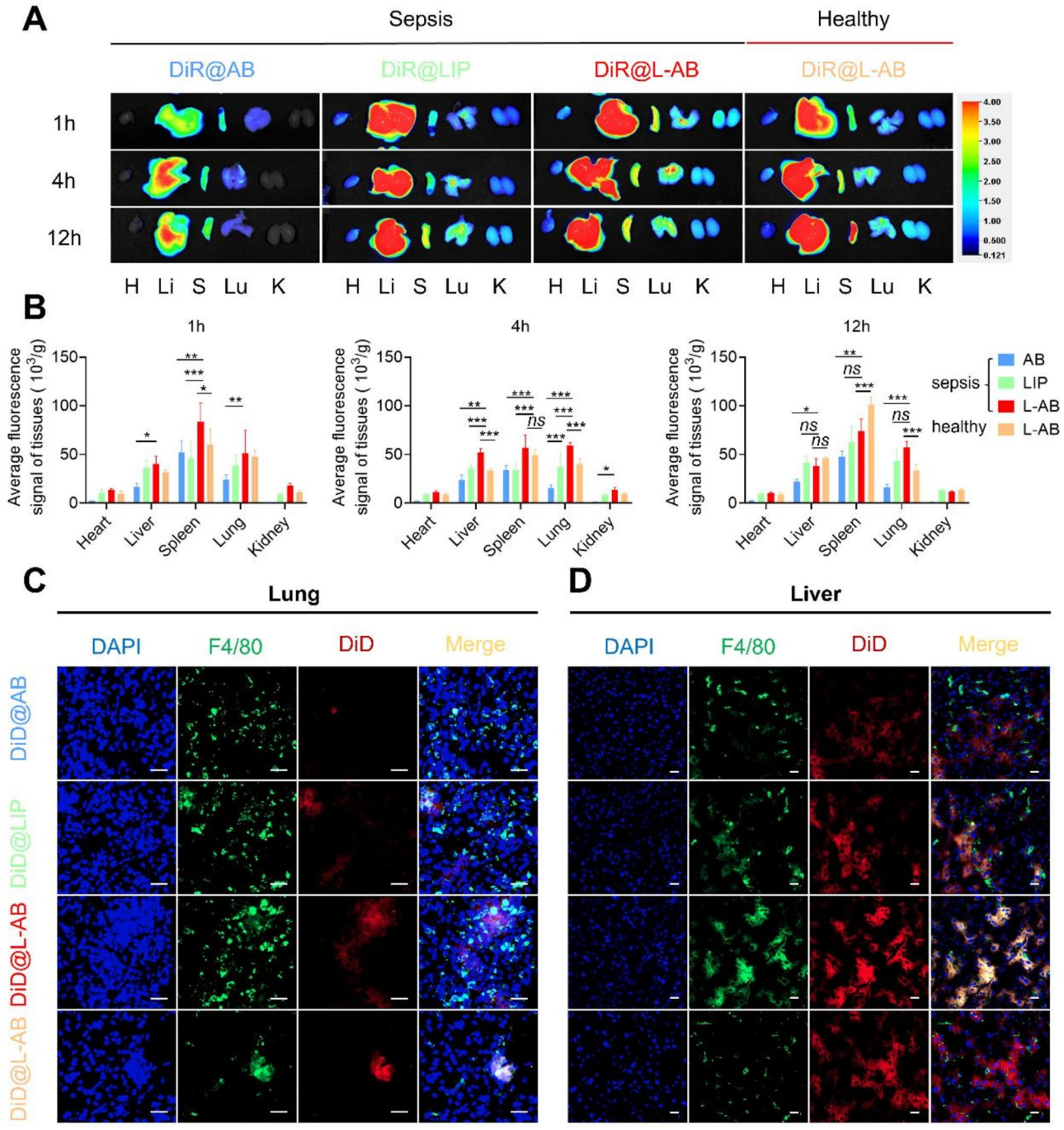

Fig. 4 Ex vivo biodistribution of L-AB. (**A**) Ex vivo biodistribution of DiR@AB, DiR@LIP, and DiR@L-AB in main organs at different time intervals via IVIS imaging. (**B**) Quantitative analysis of the DiR fluorescence signal in septic mice or healthy mice after intravenous injection of DiR@AB, DiR@LIP, and DiR@L-AB ($n = 3$). H, Li, S, Lu, and K represent heart, liver, spleen, lung, and kidney, respectively. (**C**, **D**) The localization of DiD@AB, DiD@LIP, and DiD@L-AB within the lung and liver, immunofluorescence analysis of lung and liver sections stained with F4/80. The sections were visualized using blue (DAPI), green (F4/80), and red (DiD) fluorescence, scale bar = 20 μm. Data are displayed as mean ± SD. *$P < 0.05$, **$P < 0.01$, ***$P < 0.001$

abundance of "eat me" signals present on the surface of AB, which results in their efficient elimination by the circulatory system. It is noteworthy that the MFI of L-AB in the bloodstream of septic mice was observed to be similar to that of LIP at both 4 and 12 h post intravenous administration, suggesting that L-AB exhibited a prolonged circulation capacity analogous to that of LIP.

To further confirm the uptake of L-AB by macrophages in various organs of mice, DiD-labeled AB, LIP, and L-AB were injected into septic or healthy mice via the tail vein.

Subsequently, the co-localization of L-AB with the macrophage marker F4/80 in inflamed tissues was observed by CLSM (Fig. 4C-D, S11). The results demonstrated that the expression of F4/80 was elevated in the tissues of septic mice, and L-AB exhibited enhanced co-localization with F4/80 in various inflammatory tissues, suggesting that following the distribution of L-AB to various organs, they are primarily taken up by macrophages. It was observed that the distribution of AB in the lungs was uneven, with a few macrophages accumulating a large amount of AB in their vicinity. This phenomenon might be attributed to the rapid uptake of AB by macrophages in the lungs, which may limit its further distribution. Additionally, the larger size of AB may also be a factor affecting its distribution. In addition, the percentage of DiD^+ macrophages relative to the total macrophage population was calculated, confirming the observation that DiD-labeled L-AB exhibited enhanced uptake by macrophages in the tissues of septic mice (Fig. S12). The data indicated that L-AB had the potential to combine the benefits of long-term circulation of LIP and macrophage targeting of AB, which could be advantageous for the treatment of sepsis.

Anti-inflammatory therapeutic activity of Dex@L-AB in septic mice

Subsequently, the therapeutic efficacy of Dex@L-AB was evaluated in a mouse model of LPS-induced sepsis (Fig. 5A). The mice were administered intravenously at 1 h after the establishment of the sepsis model with phosphate buffered saline (PBS), AB, free Dex, Dex@LIP or Dex@L-AB at a dosage of 1.5 mg/kg Dex. It was observed that all mice in the LPS group succumbed within 36 h (Fig. 5B). Although treatment with Dex resulted in an extension of survival time in some mice, the overall survival rate remained unchanged. The survival rate of mice in the Dex@LIP group increased to 50%, which might be attributed to the prolonged circulation and tissue

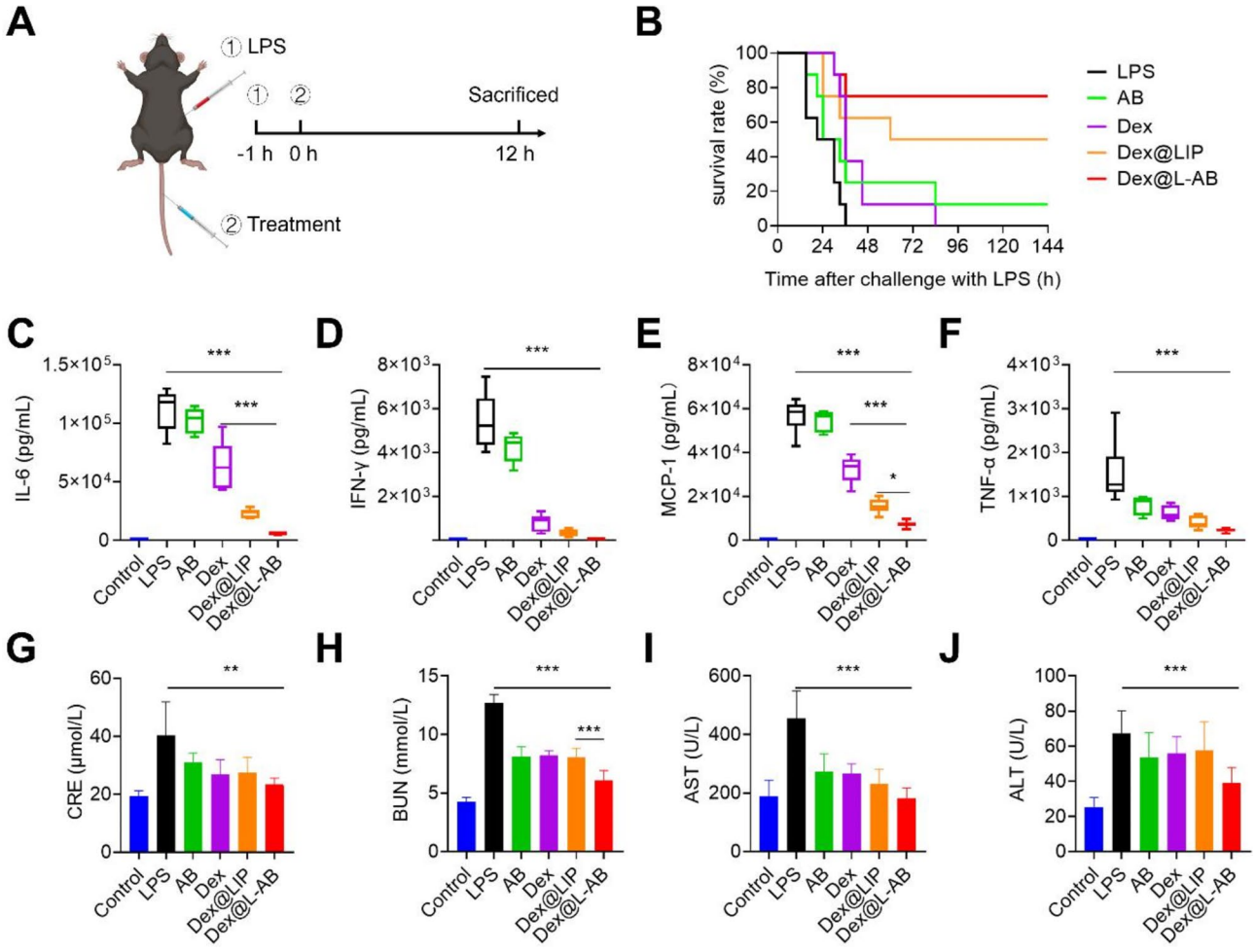

Fig. 5 Therapeutic effects of Dex@L-AB in vivo. (**A**) Experimental procedures for the LPS-induced sepsis mouse model. (**B**) Survival rate of mice in different groups ($n=7$). (**C-F**) The levels of proinflammatory cytokines IL-6, IFN-γ, MCP-1 and TNF-α in serum ($n=5$). (**G-J**) Blood biochemistry analysis of CRE, BUN, ALT and AST ($n=5$). Data are displayed as mean ± SD. $^*P<0.05$, $^{**}P<0.01$, $^{***}P<0.001$

retention time of LIP. After 144 h, only one mouse treated with AB survived (12.5%), whereas more than half of the mice treated with Dex@L-AB survived (75%), indicating that Dex@L-AB exerted a protective effect in the sepsis model. Furthermore, the cytokine storm in mice was evaluated through the measurement of serum inflammatory cytokine levels. The cytokine levels in septic mice were found to be higher than those in healthy mice. Both free Dex and Dex@LIP have been demonstrated to reduce the level of proinflammatory cytokines to a certain extent. Dex@L-AB exhibited a more significantly inhibitory effect on IL-6, MCP-1 and IL-12p70 levels in septic mice compared to Dex. Conversely, no significant difference was observed in the capacity to inhibit the levels of IFN-γ and TNF-α. The average level of those cytokines in the Dex@L-AB treated group was lower than that in the Dex@LIP treated group, suggesting that Dex@L-AB may offer a more efficacious in anti-inflammatory therapy (Fig. 5C-F, S13). Sepsis frequently results in acute impairment of the kidneys and liver, which could be evaluated via blood biochemistry and histological analysis (Fig. 5G-J). The administration of LPS notably elevated the levels of hepatic (aspartate transaminase [AST] and alanine transaminase [ALT]) and renal (blood urea nitrogen [BUN] and creatinine [CRE]) dysfunction markers in comparison to control mice. In contrast, the administration of Dex@L-AB resulted in a significant improvement in the levels of these markers, indicating its efficacy in mitigating liver and kidney damage in septic mice.

Dex@L-AB attenuated the macrophage hyperactivation in vivo

Acute lung injury (ALI) is a prevalent complication of sepsis. The pathology of ALI is characterized by the excessive activation of macrophages and the infiltration of immune cells into lung tissues [47]. To ascertain whether Dex@L-AB could suppress macrophage hyperactivation in septic mice, FCM was employed to analyze the immune cells in lung tissues. As shown in Fig. 6A-B, the ratio of $CD11b^+F4/80^+$ macrophages in lung tissues were found to be diminished by Dex@L-AB treatment, indicating that Dex@L-AB suppressed macrophage activation in the lungs of septic mice. It is well established that M2 macrophages play a pivotal role in the resolution of inflammation and the repair of damaged tissues. The present study further investigated the potential of Dex@L-AB to promote the polarization of activated macrophages toward the M2 phenotype in vivo. As shown in Fig. 6C-D, the proportion of M1 macrophages ($CD86^+$) was elevated (Fig. S14) and the proportion of M2 macrophages ($CD206^+$) was decreased in the lungs of septic mice in comparison to healthy mice. Conversely, Dex@L-AB facilitated the transformation of macrophages into M2 macrophages. Furthermore, immunofluorescence staining revealed the secretion of pro-inflammatory factor iNOS and anti-inflammatory factor Arg-1 secreted by lung cells. It was observed that Dex@L-AB decreased the secretion of iNOS and increased the expression of Arg-1, indicating that the microenvironment of inflammation might be improved by Dex@L-AB (Fig. 6E). As shown in Fig. 6F, histological examination of lung tissue sections revealed that mice in the LPS group exhibited increased neutrophil infiltration, alveolar interstitial edema and thickened alveolar walls. Conversely, the different drug treatment attenuated these pathologic manifestations, with Dex@L-AB exhibiting a better therapeutic effect. Myeloperoxidase (MPO) is a leukocyte enzyme released by activated neutrophils and monocytes. It forms free radicals and other oxidative substances that kill pathogens [48]. However, this also results in oxidative damage to host tissues at the inflammatory sites [48]. Following LPS stimulation, there was an increase in MPO levels in the lung tissue. Nevertheless, MPO levels were effectively reduced following treatment with Dex@L-AB. In summary, Dex@L-AB inhibited the excessive activation of pulmonary macrophages in septic mice, thereby suppressing the inflammatory cytokine storm and reducing lung tissue damage.

Dex@L-AB attenuated cytokine storm-associated multiple organ damage in vivo

In the event of an infection-induced cytokine storm, multiple organ damage may occur, including acute liver and kidney injury in addition to pulmonary damage [2]. Accordingly, it was also investigated whether Dex@L-AB could protect a number of organs from inflammatory damage in vivo. Following the administration of LPS, it was observed that several organs exhibited clear pathological lesions, including hemorrhage and inflammatory cell infiltration. Lesions were observed in the liver, kidney, and spleen. Furthermore, the mice that had been challenged with LPS exhibited evidence of liver necrosis, necrotic shedding of renal tubular epithelial cells forming casts, and disorganized germinal centers (Fig. 7A). In contrast, treatment with Dex@L-AB was observed to inhibit the formation of lesions in multiple organs. The excessive production of cytokine can induce cell death by triggering the overproduction of ROS and subsequent activation of pro-apoptotic signals, which ultimately accelerates the onset and progression of organ failure [49]. Furthermore, apoptosis was monitored through immunofluorescence in various tissue sections. As shown in Fig. 7B, the number of apoptotic cells in the major organs (lung, liver and spleen) of LPS-treated mice was significantly elevated in comparison to the control group. However, this elevation was ameliorated by treatment with Dex@L-AB. In conclusion, Dex@L-AB may prove

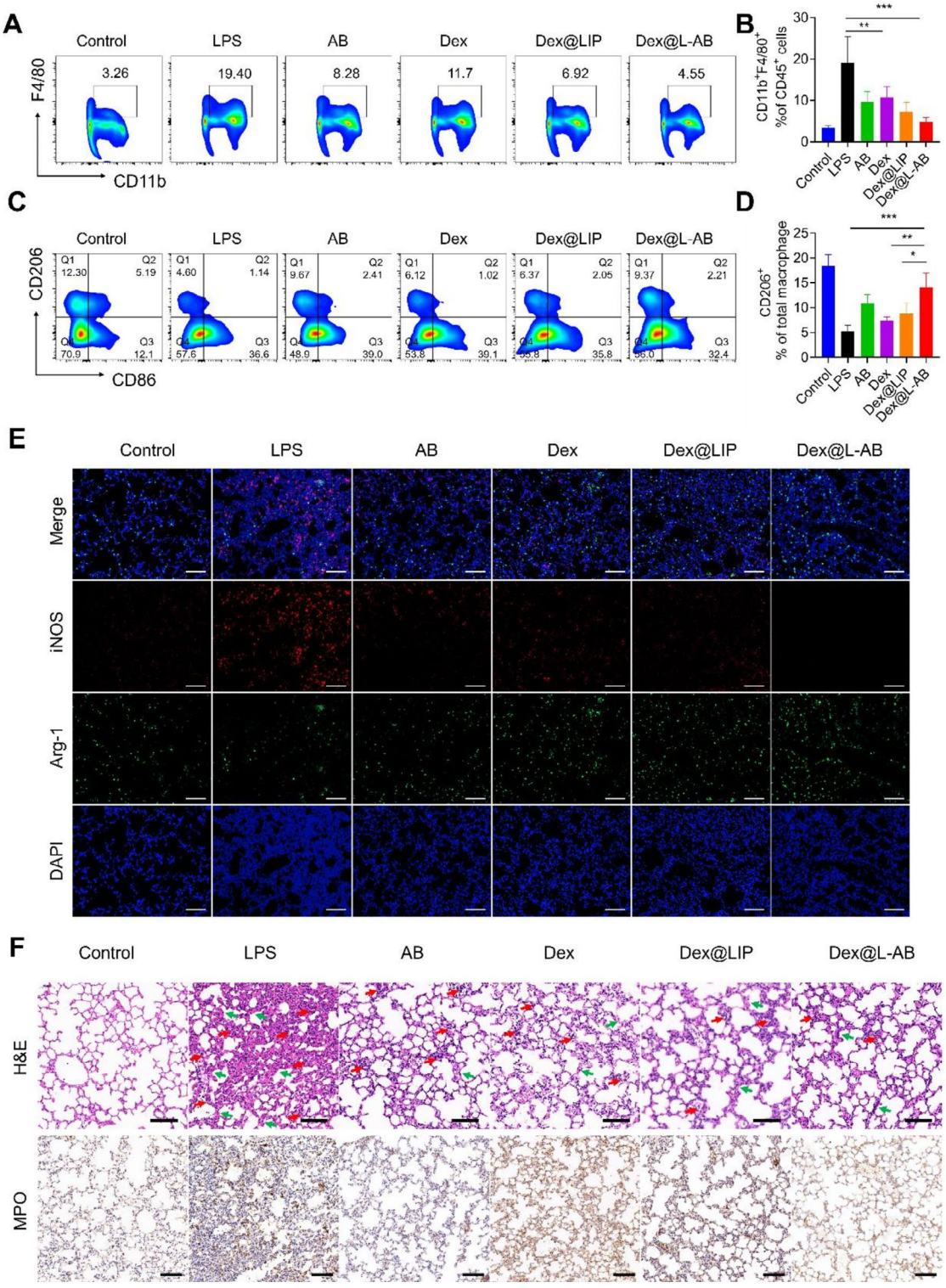

Fig. 6 Therapeutic effect for experiencing sepsis-induced acute lung injury. (**A**) Representative plots of $CD11b^+$ $F4/80^+$ cells as a percentage of the total $CD45^+$ cells population and (**B**) corresponding quantification results after various treatments ($n = 5$). (**C**) Representative plots of $CD206^+$ cells as a percentage of the total macrophages population and (**D**) corresponding quantification results after various treatments ($n = 5$). (**E**) Representative fluorescence images of iNOS and Arg-1 in lung tissue after different treatments. (**F**) H&E staining and IHC staining of MPO of lung after different treatments (red arrows indicate inflammatory cells infiltration, green arrows indicate thickened alveolar walls). Scale bar = 100 μm. Data are displayed as mean ± SD. $^*P < 0.05$, $^{**}P < 0.01$, $^{***}P < 0.001$

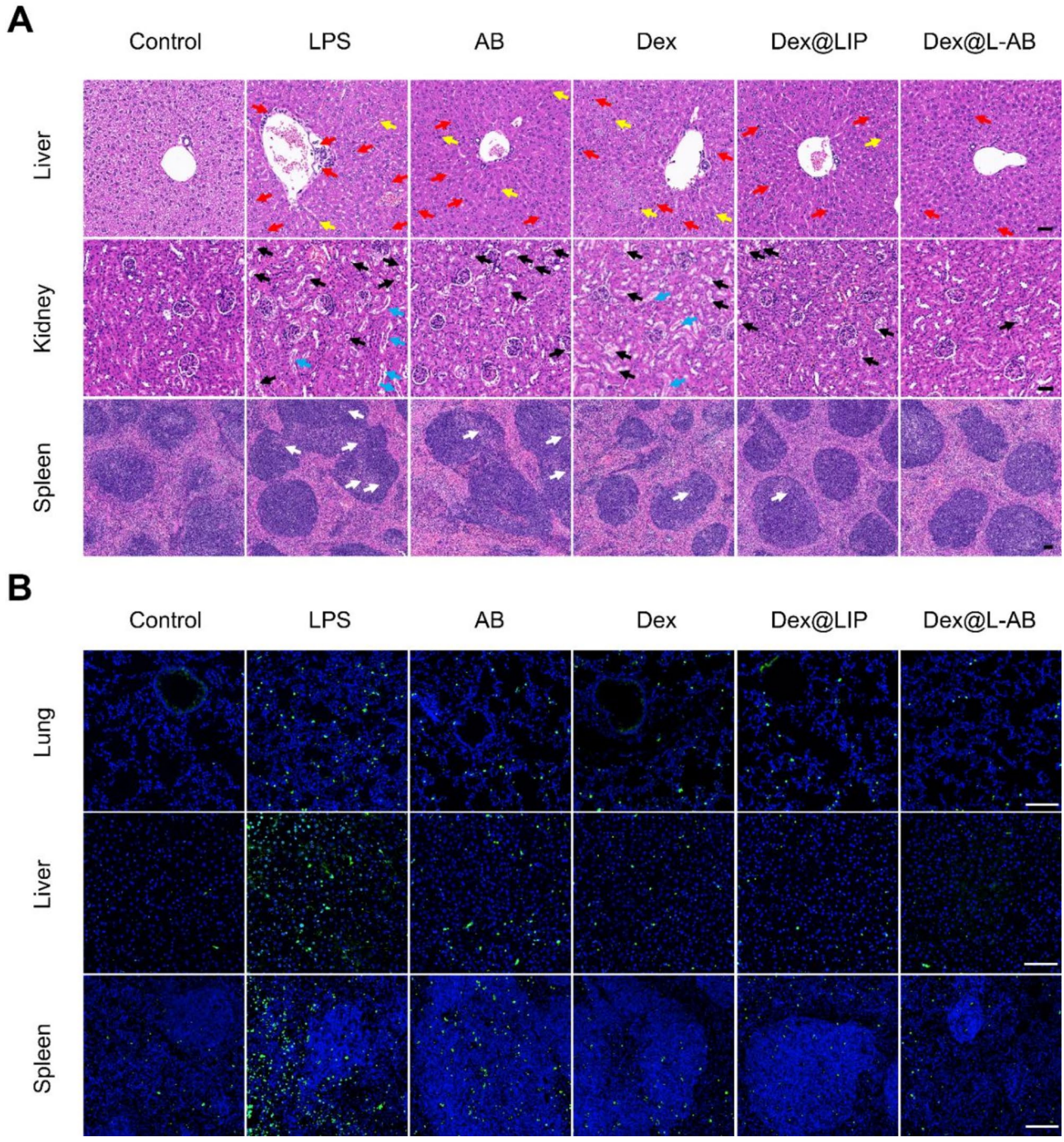

Fig. 7 Dex@L-AB relieved tissue injuries and cellular apoptosis of septic mice. (**A**) H&E staining of liver, kidney and spleen tissues. Red arrows indicate inflammatory cells infiltration; yellow arrows indicate liver necrosis cells; black arrows indicate vacuolated renal tubules; blue arrows indicate necrotic shedding of renal tubular epithelial cells to form casts and white arrows indicate disorganized germinal centers. (**B**) TUNEL staining of lung, liver and spleen tissues (green fluorescence: TUNEL positive cells; blue fluorescence: cell nucleus). Scale bar = 100 μm

an effectively means of reducing organ damage in septic mice, thereby contributing to an improvement in survival rates.

The present study demonstrated that Dex@L-AB mitigated excessive inflammatory responses in septic mice mainly by inhibiting macrophage activation in vivo. However, sepsis exerts direct or indirect detrimental effects on nearly all types of immune cells [50]. Consequently, further investigation is required to elucidate the impact of Dex@L-AB on other immune cell populations in septic mice. Furthermore, although it has been demonstrated that the majority of L-AB is the consequence

of the fusion of AB and LIP, there may be instances where AB or LIP have not undergone fusion. Further research is required to develop effective purification and removal techniques for these components warrants.

Conclusion

In summary, inspired by the targeted clearance of AB by macrophages, we developed L-AB by fusing AB derived from M2-type macrophages with liposomes to facilitate the delivery of Dex for the treatment of sepsis. L-AB inherits certain "eat me" signals from AB, promoting enhanced uptake by macrophages, while also effectively encapsulating Dex. Dex@L-AB exhibited better anti-inflammatory effects in vitro and in vivo. In the treatment of septic mice, Dex@L-AB more effectively inhibited cytokine storms compared to the free drug, thereby reducing organ damage and improving the survival rate of the mice. This work offers novel insights into the treatment of sepsis.

Materials and methods

Materials

DOPC (LP-R4-070), DSPE-PEG2000 (R-1028–2 K), and cholesterol (R-H-100001) were purchased from Xi'an Ruixi Biological Technology Co. Ltd. Recombinant murine IL-4 was purchased from Peprotech (USA). Macrophage colony-stimulating factor (M-CSF, RP01216) was purchased from Abclonal (China). LPS (L2630) was purchased from Sigma-Aldrich (USA). Dex (S17003) was purchased from Shanghai Yuanye Bio-Technology (China). Penicillin-streptomycin solution, Dulbecco's modified Eagle medium (DMEM), PBS, and fetal bovine serum (FBS) were purchased from Hyclone (USA). RIPA lysis buffer (P0013B), DAPI (C1002), bicinchoninic acid (BCA) assay kit (P0012S), ROS assay kit (S0033S), and NO assay kit (S0021S) were purchased from Beyotime (China). DiO (HY-D0969), DiD (HY-D1028), DiI (HY-D0083), DiR (HY-D1048), Staurosporine (STS, HY-15141) and protease inhibitor cocktail (HY-K0010) were purchased from MedChemExpress (USA). Annexin V-Alexa Fluor 647/PI apoptosis detection kit (40304ES50) and gold band plus three-color regular range protein marker (20350ES72) were brought from Yeasen (Shanghai, China). The CBA mouse inflammation kit (552364) was purchased from BD Pharmingen (USA). Other chemical reagents were obtained from Sinopharm Chemical Reagent Co., Ltd. (China).

Cell culture

The murine RAW264.7 macrophage cells (Chinese Academy of Sciences, Shanghai, China) were cultured in DMEM supplemented with 10% FBS (V/V) at 37 °C in 5% CO_2 humidified air. The RAW264.7 cells were treated with 20 ng/mL IL-4 for 48 h in order to induce the M2 phenotype.

Animals

Male C57 BL/6 mice (8 to 9 weeks old) were purchased from Henan Sikebas Biotechnology Co., Ltd. (China) and maintained under specific pathogen-free conditions in the Animal Centre of Huazhong University of Science and Technology (HUST).

AB isolation

M2 macrophages were starved in serum-free medium and treated with STS (0.5 mM) for a duration of 12 h to induce apoptosis. Subsequently, the culture medium was harvested and centrifuged at 300 g for 10 min to remove cellular components and debris. The resulting supernatant was then centrifuged at 3000 g for 20 min to concentrate the AB into a particulate form. These particles were then resuspended in PBS and stored at -80 °C for subsequent experimental analyses. The protein content of the AB was quantified using the BCA protein detection kit. Additionally, AB was stained with Annexin-V-Alexa Fluor 647 labeling reagent, and the resulting solution was observed by CLSM (AX, Nikon, Tokyo, Japan). Fluorescent dyes (DiO, DiD, DiI, or DiR) were used to label the AB through the co-incubation at 37 °C for 30 min, and the free dye was removed by centrifugation at 3000 g for 20 min.

Preparation of L-AB

Liposomes were prepared using the thin film hydration method. The components DOPC, cholesterol, and DSPE-PEG2000 were dissolved in 3 mL of chloroform at a molar ratio of 8:8:1. The solvent was then evaporated using a rotary evaporator in a round flask followed by the hydration with 2 mL of PBS or with 2 mL of PBS containing 250 μg of AB proteins at 45 °C for half an hour. The suspension was then vortexed and sonicated for 10 min. Subsequently, the lipid suspension was extruded 11 times through 1 and 0.4 μm polycarbonate membrane filters using a mini extruder to obtain uniform LIP or L-AB. For fluorescence visualization, fluorescent dyes (DiO, DiD, DiI, or DiR) were added to during the lipid film fabrication process, with the intention of labeling the LIP or L-AB.

Characterization of AB, LIP and L-AB

The hydrodynamic diameter and zeta potential of AB, LIP and L-AB were evaluated by DLS (Brookhaven Instruments, NY, USA). The morphology of AB, LIP, and L-AB was analyzed by TEM at 100 kV using the HT7800(HITACHI, Japan). For TEM analysis, the samples were diluted to an appropriate concentration and 10 μL of each was applied to the grid. Following a 30-min

precipitation period, the remaining liquid was removed and 10 μL of 2% uranyl acetate was added for a further 30 s.

Verification of L-AB fusion

In order to assess the fusion efficiency of AB and LIs, DiI-labeled LIP (DiI@LIP) and DiO-labeled AB (DiO@AB) were employed to create co-labeled L-AB during the hydration and fusion process. A physical mixture of DiI@LIP and DiO@AB was used as a control. The incorporation of fluorescently labeled AB and LIP was visualized using a Full Spectrum Ultra High Resolution Laser Confocal Scanning System (Stellaris STED, Leica, Germany). Additionally, FRET technology was utilized to investigate the fusion of membranes. In brief, AB were labeled with DiI (λex/λem = 549/565nm) and DiD (λex/λem = 644/663 nm). Afterward, LIP was subjected to fluorochrome-tagged AB at varying mass proportions to facilitate hydration and co-fusion. Subsequently, the hybrid dye-labeled L-AB were examined at λex = 525 nm, and the fluorescence spectra were recorded ranging from 550 to 750 nm.

Protein analysis of AB and L-AB

To investigate the general retention, M0/M2/apoptotic M2 cells, AB, and L-AB were lysed with RIPA lysis buffer. The extracted proteins were denatured at 95 °C for 7 min. The proteins were loaded onto a 10% SDS-PAGE gel. For the purpose of studying specific protein expression, proteins were loaded onto 10% SDS-PAGE gels and subsequently transferred to a polyvinylidene fluoride (PVDF) transfer membrane. The membrane was blocked for 1 h with 5% milk, after which it was incubated overnight at 4 °C with primary antibodies, including anti-CD206 (1:1000, CST, 24595), anti- Caspase-3 (1:1000, CST, 14220), anti- Cleaved caspase-3 (1:1000, CST, 9664), anti-CD9 (1:1000, CST, 13174), and anti-β-actin (1:1000, CST, 58169). Following three washes in TBST, the membranes were incubated with fluorescently labeled secondary antibodies at room temperature for 2 h. Subsequently, they were visualized using the Odyssey DLx Imaging System (LI-COR, USA).

Nano flow cytometric analysis

The analysis of cellular membrane protein and phosphatidylserine proportion and orientation of AB in L-AB were examined via NanoFCM (NanoFCM Inc., Xiamen, China). Specifically, Alexa Fluor 647-Annexin V (Yeasen, 40304ES50) and FITC-CD11b (BD Pharmingen, 101205) were incubated with the fabricated L-AB for 30 min in the dark, after which the proportion of phosphatidylserine and CD11b on the carrier surface was detected by NanoFCM.

Cell viability assay

The MTT assay was performed to assess the cell viability of L-AB. LIP and AB were used as controls. The RAW264.7 cells were cultured in 96-well plates and treated with different concentrations of LIP, AB, and L-AB were treated for 24 h. Subsequently, an MTT solution was added for a period of 4 h. Finally, the absorbance at 490 nm was documented after dissolving the formazan crystals with DMSO.

In vitro cellular uptake

A fluorescence microscope and FCM (Accuri C6, BD) were used to investigate the cellular uptake behavior. RAW264.7 cells were seeded overnight in 24-well plates. Subsequently, DiD@AB, DiD@LIP or DiD@L-AB were incubated with cells for 1, 3–5 h. Following this, the cells were washed and fixed, with the nucleus stained with DAPI before being subjected to fluorescence microscopy (Olympus, Japan). Following incubation with DiD@AB, DiD@LIP, or DiD@L-AB, the cells were harvested, washed, and resuspended in PBS for subsequent analysis by FCM. At the predetermined time, the cells were collected and analyzed by FCM.

To further elucidate the factors influencing the phagocytosis of L-AB by macrophages, L-AB labeled with DiD was resuspended in a 100 μL calcium-containing buffer with ANXA5 protein and incubated at room temperature for 30 min prior to incubation with RAW264.7 cells. Additionally, RAW264.7 cells were pretreated with 25 μM UNC2250 for 4 h, after which L-AB was introduced into the culture system. Following a 3-hour incubation period, RAW264.7 cells were collected, washed with PBS, and subsequently analyzed by FCM.

Investigation of uptake mechanism

After pre-treating RAW264.7 cells with different inhibitors (40 μM Chlorpromazine, 0.5 mM Sucrose, 10 mM M-β-CD, 0.1 mM Amiloride) for 1 h, DiD@L-AB was added and incubated for 5 h, and the cells were collected for FCM.

In vivo biodistribution of AB, LIP, L-AB

To investigate the ex vivo biodistribution of LIP, AB and L-AB, the sepsis animal model was first constructed by administering LPS (20 mg/kg, intraperitoneally) to male C57BL/6 mice. After 1 h, DiR-labeled AB, LIP, and L-AB (at an equal DiR dosage of 0.5 mg/kg) were prepared and injected intravenously for the purpose of investigating biodistribution. After 1, 4, or 12 h, the mice were sacrificed and perfused. The major organs and blood were then harvested and processed using IVIS imaging systems (IVIS Lumina XR system, Trilogy, LI-COR). To examine the cellular uptake of AB, LIP, and L-AB by macrophages in the indicated tissue, tissue sections from

mice treated with DiD-labeled AB, LIP, and L-AB were prepared and additionally incubated with an anti-F4/80 antibody (1:100, CST, 70076T), followed by DAPI staining. In addition, to ascertain the disparity in the biodistribution of L-AB between septic mice and healthy mice, fluorescence-labeled L-AB were administered concurrently to healthy mice, who served as a control. All images were obtained using the Olympus SLIDEVIEW VS200 (Olympus, Japan).

Dex loading and in vitro cumulative release study

Dex was loaded into LIP or L-AB through the thin-film hydration method. Briefly, Dex was dissolved in methanol and added to the lipid solution in the aforementioned ratio. The drug-to-lipid ratio of Dex to total lipid was 1 mg/30 mg. The solvent was then evaporated in a round flask using a rotary evaporator. The preparation of Dex-encapsulated LIP (Dex@LIP) or L-AB (Dex@L-AB) followed the same procedure as that used for the preparation of LIP and L-AB, with the exception of the removal of unencapsulated Dex, which was achieved through dialysis tube (3500 MWCO) in PBS. The encapsulation efficiency was calculated by the following formula:

$Encapusulation\ efficiency$ (100%)=(Weight of encapuslated drug)/(Weight of total added drug) × 100%.

The in vitro Dex release was investigated by a dialysis method. In brief, dialysis tubes containing 1 mL of each sample were immersed in 30 mL of PBS medium (pH 7.4). The samples were then incubated at 37 °C with shaking at 100 rpm. At predetermined time points, the released media was removed and replaced with fresh media. The concentration of released Dex in the medium was determined by HPLC using a C18 column. The eluent consisted of was acetonitrile (0.05% TFA)/H_2O (0.05% TFA) (0 ~ 10 min, from 20/80 to 60/40) and the detection wavelength was set at 240 nm.

Anti-inflammatory effect analysis in vitro

To induce a pro-inflammatory phenotype, RAW264.7 cells were incubated for 24 h at 37 °C with 100 ng/mL LPS and 30 ng/mL INF-γ. To remove the inducer and other components, the pro-inflammatory RAW264.7 cells were washed three times with PBS. Subsequently, the AB, Dex, Dex@LIP, and Dex@L-AB were dispersed in a blank media. After incubation for 24 h, the culture supernatant was collected and centrifuged at 10,000 rpm for 10 min at 4 °C. The isolated supernatant was transferred to a low-adsorption centrifugal tube and then detected for nitrite and cytokine levels. The Griess reagent kit was used to detect NO content. In accordance with the manufacturer's instructions, the level of NO secretion was quantified by measuring the absorbance at 540 nm. Meanwhile, a CBA was employed to perform the cytokine (IL-6, TNF-α, INF-γ) assay.

Intracellular ROS evaluation

RAW264.7 cells were seeded into 24-well plate and cultured overnight under inflammatory stimulation (100 ng/mL LPS + 30 ng/mL INF-γ). The cells were subsequently treated with a range of drugs and subsequently labeled with DCFH-DA. After 30 min, the cells were washed twice to remove any residual free ROS-sensitive probe. The ROS levels were then quantified via FCM.

Ability of Dex@L-AB to inhibit nuclear translocation of p65

RAW264.7 macrophages were cultured on coverslips, treated with 200 ng/mL LPS for 12 h, and subsequently incubated with various formulations for 24 h. Subsequently, the cells were gently rinsed with PBS, fixed in 4% paraformaldehyde, and permeabilized with 0.1% Triton X-100 for 15 min. After blocking with 5% BSA for 1 h, the coverslips were incubated with rabbit anti-p65 antibody (1:100, CST, 8242) for 3 h, followed by a 1-hour incubation with Cy3-labeled secondary antibody (1:200, Beyotime, A0516). The nuclei were then counterstained with DAPI, and the cells were visualized using CLSM.

In vivo anti-inflammation efficiency of Dex@L-AB

To induce sepsis, mice were intraperitoneally injected with LPS at a dose of 20 mg kg^{-1}. After 1 h, the mice were randomly grouped (n = 8/group) and intravenously injected with different formulations. The following formulations were evaluated: PBS, AB, Dex, Dex@LIP, Dex@L-AB. All formulations were found to be equivalent to a dose of Dex of 1.5 mg/kg. The behavioral characteristics of mice were monitored and recorded throughout the duration of the experiments. The mice were subsequently sacrificed 12 h later. Blood samples were collected, centrifuged, and analyzed for cytokines (TNF- α, INF-γ, MCP-1, IL-6 and IL-12p70), hepatic (AST and ALT) and renal (BUN and CRE) function indicators.

Fraction of immunocytes and macrophages in lung

The lung tissue of mice was crushed and homogenized with nylon gauze to obtain a single-cell suspension. After being treated with red blood cell lysis buffer and blocking with anti-CD16/CD32 (1:100, Biolegend, 101302), the cell suspensions were stained with anti-CD45-PerCP-Cy5.5(1:100, Biolegend, 103132), anti-CD11b-FITC (1:100, Biolegend, 101206), and anti-F4/80-APC (1:100, BD Pharmingen, 566787) at 4 °C for 1 h. After repeated washing with PBS, the cells were analyzed with a Sony ID7000 multicolor cell analyzer. The data were subjected to analysis using the FlowJo software, version X. Tissues (liver, spleen, left lung and kidney) were collected, fixed, embedded and sectioned for hematoxylin and eosin (H&E) staining, immunohistochemical staining of MPO (1:500, Servicebio, GB150006-100) for the evaluation of neutrophil infiltration. IF staining of Arg-1 (1:500,

Servicebio, GB11285-100) and iNOS (1:500, Servicebio, GB11119-100) was performed for the evaluation of pro-inflammatory and anti-inflammatory substance secretion in tissues.

TUNEL staining of tissues

TUNEL staining was carried out with a commercial kit (Promega, Madison, WI, USA) following the manufacturer's instructions, and nuclei were stained with DAPI. The stained lung, liver and spleen sections were observed under a fluorescence microscope.

Statistical analysis

All results were presented as mean ± standard deviation (SD). One-way ANOVA or Student's t-test was used for different analysis among groups with GraphPad Prism 8.0 software. Statistical significance was present as $^{*}p<0.05$; $^{**}p<0.01$; $^{***}p<0.001$.

Abbreviations

AB	Apoptotic bodies
L-AB	Apoptotic body based biomimetic hybrid nanovesicles
Dex	Dexamethasone
Dex@L-AB	Dex-loaded L-AB
MODS	Multiple organ dysfunction syndrome
IL-6	Interleukin-6
TNF-α	Tumor necrosis factor-α
MCP-1	Monocyte chemotactic protein 1
EV	Extracellular vesicles
PS	Phosphatidylserine
M2-EV	M2 macrophages-derived EV
ARDS	Acute respiratory distress syndrome
TEM	Transmission electronic microscopy
PDI	Polydispersity index
DLS	Dynamic light scattering
FRET	Förster resonance energy transfer
CLSM	Confocal laser scanning microscope
FTIR	Fourier Transform Infrared
SDS-PAGE	Sodium dodecyl sulfate-polyacrylamide gel electrophoresis
MFI	Mean fluorescence intensity
M-β-CD	Methyl-β-cyclodextrin
FCM	Flow cytometry
MPO	Myeloperoxidase
HPLC	High-performance liquid chromatography
FBS	Fetal bovine serum
BCA	Bicinchoninic acid
ROS	Reactive oxygen species
LPS	Lipopolysaccharides
IFN-γ	Interferon-γ
CBA	Cytometric bead array
NF-κB	Nuclear factor kappa-B
AST	Aspartate transaminase
ALT	Alanine transaminase
BUN	Blood urea nitrogen
CRE	Creatinine
ALI	Acute lung injury
M-CSF	Macrophage colony-stimulating factor
PBS	Phosphate buffered saline
STS	Staurosporine
H&E	Hematoxylin and eosin
TUNEL	Transferase dUTP nick end labeling

Supplementary Information

The online version contains supplementary material available at https://doi.org/10.1186/s12951-024-03058-3.

Supplementary Material 1

Acknowledgements

The authors thank the Analytical and Testing Center of HUST for the TEM test. The authors thank the Medical Subcenter of HUST Analytical & Testing Center for providing FCM tests. The authors also thank the Laboratory Animal Center of HUST for mouse housing. The authors thank Figdraw platform of the Home for Researchers (www.home-for-researchers.com) for visualization.

Author contributions

Hongbing Lan: Conceptualization, Investigation, Methodology, Writing – review & editing. Zhanhao Zhou: Conceptualization, Investigation, Methodology. Qian Hu: Methodology. Qi Xie: Methodology. Xiaonan Li: Validation, Methodology. Tianyi Tian: Methodology. Yi Wang: Methodology. Conglian Yang: Methodology. Li Kong: Methodology. Dehao Fu: Conceptualization, Supervision, Writing – review & editing. Yuanyuan Guo: Conceptualization, Supervision, Funding acquisition, Writing – review & editing. Zhiping Zhang: Conceptualization, Supervision, Funding acquisition, Writing – review & editing. All authors have reviewed and approved the final manuscript.

Funding

This work was supported by the National Natural Science Foundation of China (No.82373816 and No.82173760) and the Hubei Provincial Natural Science Foundation Joint Fund for Innovation and Development Project (No. 2024AFD347) and the Intramural Research Program of Liyuan Hospital (No. 2023LYYYGZRP0002).

Data availability

No datasets were generated or analysed during the current study.

Declarations

Ethics approval and consent to participate

All the animal experiments were approved by the Experimental Animal Center of HUST. Animal experiments were carried out in compliance with the Guide for the Animals Care and Ethics Committee of HUST, with the assigned [2023] IACUC number (3678).

Consent for publication

All authors consent for publication.

Competing interests

The authors declare no competing interests.

Received: 29 July 2024 / Accepted: 2 December 2024
Published online: 19 December 2024

References

1. Cecconi M, Evans L, Levy M, Rhodes A. Sepsis and septic shock. Lancet. 2018;392(10141):75–87.
2. Singer M, Deutschman CS, Seymour CW, Shankar-Hari M, Annane D, Bauer M, Bellomo R, Bernard GR, Chiche J-D, Coopersmith CM, et al. The third international consensus definitions for sepsis and septic shock (Sepsis-3). JAMA. 2016;315(8):801–10.
3. Coperchini F, Chiovato L, Croce L, Magri F, Rotondi M. The cytokine storm in COVID-19. An overview of the involvement of the chemokine/chemokine-receptor system. Cytokine Growth Factor Rev. 2020;53:25–32.
4. Zheng X, Xing YJ, Sun K, Jin HZ, Zhao W, Yu F. Combination therapy with resveratrol and celastrol using folic acid-functionalized exosomes enhances the therapeutic efficacy of sepsis. Adv Healthc Mater. 2023;12(27):2301243.

5. Lee J, Son W, Hong J, Song Y, Yang CS, Kim YH. Down-regulation of TNF-α via macrophage-targeted RNAi system for the treatment of acute inflammatory sepsis. J Controlled Release. 2021;336:344–53.
6. van Niel G, D'Angelo G, Raposo G. Shedding light on the cell biology of extracellular vesicles. Nat Rev Mol Cell Biol. 2018;19(4):213–28.
7. Elsharkasy OM, Nordin JZ, Hagey DW, de Jong OG, Schiffelers RM, Andaloussi SEL, Vader P. Extracellular vesicles as drug delivery systems: why and how? Adv Drug Del Rev. 2020;159:332–43.
8. Herrmann IK, Wood MJA, Fuhrmann G. Extracellular vesicles as a next-generation drug delivery platform. Nat Nanotechnol. 2021;16(7):748–59.
9. Cheng L, Hill AF. Therapeutically harnessing extracellular vesicles. Nat Rev Drug Discov. 2022;21(5):379–99.
10. Yu L, Zhu G, Zhang Z, Yu Y, Zeng L, Xu Z, Weng J, Xia J, Li J, Pathak JL. Apoptotic bodies: bioactive treasure left behind by the dying cells with robust diagnostic and therapeutic application potentials. J Nanobiotechnol. 2023;21(1):218.
11. Tian T, Zhu Y-L, Zhou Y-Y, Liang G-F, Wang Y-Y, Hu F-H, Xiao Z-D. Exosome uptake through clathrin-mediated endocytosis and macropinocytosis and mediating miR-21 delivery. J Biol Chem. 2014;289(32):22258–67.
12. Depraetere V. Eat me' signals of apoptotic bodies. Nat Cell Biol. 2000;2(6):E104.
13. Segawa K, Nagata S. An apoptotic 'Eat me' signal: phosphatidylserine exposure. Trends Cell Biol. 2015;25(11):639–50.
14. Li X, Li S, Fu X, Wang Y. Apoptotic extracellular vesicles restore homeostasis of the articular microenvironment for the treatment of rheumatoid arthritis. Bioact Mater. 2024;35:564–76.
15. Liu D, Kou X, Chen C, Liu S, Liu Y, Yu W, Yu T, Yang R, Wang R, Zhou Y, Shi S. Circulating apoptotic bodies maintain mesenchymal stem cell homeostasis and ameliorate osteopenia via transferring multiple cellular factors. Cell Res. 2018;28(9):918–33.
16. Medina CB, Mehrotra P, Arandjelovic S, Perry JSA, Guo Y, Morioka S, Barron B, Walk SF, Ghesquière B, Krupnick AS, et al. Metabolites released from apoptotic cells act as tissue messengers. Nature. 2020;580(7801):130–5.
17. Huynh MLN, Fadok VA, Henson PM. Phosphatidylserine-dependent ingestion of apoptotic cells promotes TGF-β1 secretion and the resolution of inflammation. J Clin Invest. 2002;109(1):41–50.
18. Li MO, Sarkisian MR, Mehal WZ, Rakic P, Flavell RA. Phosphatidylserine receptor is required for clearance of apoptotic cells. Science. 2003;302(5650):1560–3.
19. Zhou M, Li YJ, Tang YC, Hao XY, Xu WJ, Xiang DX, Wu JY. Apoptotic bodies for advanced drug delivery and therapy. J Controlled Release. 2022;351:394–406.
20. Zhao DY, Tao WH, Li SH, Chen Y, Sun YH, He ZG, Sun BJ, Sun J. Apoptotic body-mediated intercellular delivery for enhanced drug penetration and whole tumor destruction. Sci Adv. 2021;7(16):eabg0880.
21. Bose RJC, Tharmalingam N, Garcia Marques FJ, Sukumar UK, Natarajan A, Zeng Y, Robinson E, Bermudez A, Chang E, Habte F, et al. Reconstructed apoptotic bodies as targeted Nano Decoys to treat intracellular bacterial infections within macrophages and cancer cells. ACS Nano. 2020;14(5):5818–35.
22. Bao LL, Dou G, Tian R, Lv YJ, Ding F, Liu SY, Zhao RF, Zhao L, Zhou J, Weng L, et al. Engineered neutrophil apoptotic bodies ameliorate myocardial infarction by promoting macrophage efferocytosis and inflammation resolution. Bioact Mater. 2022;9:183–97.
23. Dou G, Tian R, Liu X, Yuan P, Ye Q, Liu J, Liu S, Zhou J, Deng Z, Chen X, et al. Chimeric apoptotic bodies functionalized with natural membrane and modular delivery system for inflammation modulation. Sci Adv. 2020;6(30):eaba2987.
24. Huang ZW, Li XZ, Yu DD, Wang HC, Chun C, Zhao YZ. Efferocytosis-inspired biomimetic nanoplatform for targeted acute lung injury therapy. Adv Healthc Mater. 2024;13(13):2304304.
25. Hu M, Zhang J, Kong L, Yu YL, Hu Q, Yang T, Wang Y, Tu K, Qao Q, Qin XY, Zhang ZP. Immunogenic hybrid nanovesicles of liposomes and tumor-derived nanovesicles for cancer immunochemotherapy. ACS Nano. 2021;15(2):3123–38.
26. Qiao Q, Liu X, Cui KX, Li XA, Tian TY, Yu YL, Niu BN, Kong L, Yang CL, Zhang ZP. Hybrid biomimetic nanovesicles to Drive High Lung Biodistribution and prevent cytokine storm for ARDS Treatment. ACS Nano. 2022;16(9):15124.
27. Li XN, Qiao Q, Liu X, Hu Q, Yu YL, Qin XY, Tian TY, Tian YM, Ou XJ, Niu BN, et al. Engineered biomimetic nanovesicles based on neutrophils for hierarchical targeting therapy of acute respiratory distress syndrome. ACS Nano. 2024;18(2):1658–77.
28. Yang J, Huang XF, Yu Q, Wang SB, Wen XH, Bai SJ, Cao LX, Zhang K, Zhang SF, Wang XG, et al. Extracellular vesicles derived from M2-like macrophages alleviate acute lung injury in a mir-709-mediated manner. J Extracell Vesicles. 2024;13(4):12437.
29. Wang YZ, Liu SY, Li L, Li L, Zhou XL, Wan MH, Lou P, Zhao M, Lv K, Yuan YJ, et al. Peritoneal M2 macrophage-derived extracellular vesicles as natural multitarget nanotherapeutics to attenuate cytokine storms after severe infections. J Controlled Release. 2022;352:118–32.
30. Jiao Y, Zhang T, Liu M, Zhou LY, Qi MZ, Xie X, Shi XY, Gu XP, Ma ZL. Exosomal PGE2 from M2 macrophages inhibits neutrophil recruitment and NET formation through lipid mediator class switching in sepsis. J Biomed Sci. 2023;30(1):62.
31. Ledford H. Coronavirus breakthrough: dexamethasone is first drug shown to save lives. Nature. 2020;582(7813):469–469.
32. Sinha S, Rosin NL, Arora R, Labit E, Jaffer A, Cao L, Farias R, Nguyen AP, de Almeida LGN, Dufour A, et al. Dexamethasone modulates immature neutrophils and interferon programming in severe COVID-19. Nat Med. 2022;28(1):201–11.
33. Boada-Romero E, Martinez J, Heckmann BL, Green DR. The clearance of dead cells by efferocytosis. Nat Rev Mol Cell Biol. 2020;21(7):398–414.
34. Liu X, Qiao Q, Li XN, Ou XJ, Cui KX, Niu BN, Yang CL, Kong L, Zhang ZP. Apoptotic neutrophil-mediated inflammatory microenvironment regulation for the treatment of ARDS. Nano Today. 2023; (52): 101946.
35. Xu H, Liao C, Liang S, Ye BC. A novel peptide-equipped exosomes platform for delivery of antisense oligonucleotides. ACS Appl Mater Interfaces. 2021;13(9):10760–7.
36. Zou J, Shi M, Liu X, et al. Aptamer-Functionalized exosomes: elucidating the Cellular Uptake mechanism and the potential for Cancer-targeted chemotherapy. Anal Chem. 2019;91(3):2425–30.
37. Mulcahy LA, Pink RC, Carter DR. Routes and mechanisms of extracellular vesicle uptake. J Extracell Vesicles. 2014;3. https://doi.org/10.3402/jev.v3.24641.
38. Ogden CA, deCathelineau A, Hoffmann PR, et al. C1q and mannose binding lectin engagement of cell surface calreticulin and CD91 initiates macropinocytosis and uptake of apoptotic cells. J Exp Med. 2001;194(6):781–95.
39. Hoffmann PR, deCathelineau AM, Ogden CA, et al. Phosphatidylserine (PS) induces PS receptor-mediated macropinocytosis and promotes clearance of apoptotic cells. J Cell Biol. 2001;155(4):649–59.
40. Brodeur A, Migneault F, Lanoie M, et al. Apoptotic exosome-like vesicles transfer specific and functional mRNAs to endothelial cells by phosphatidylserine-dependent macropinocytosis. Cell Death Dis. 2023;14(7):449.
41. Zhao M, Wang YZ, Li L, Liu SY, Wang CS, Yuan YJ, Yang G, Chen YN, Cheng JQ, Lu YR, Liu JP. Mitochondrial ROS promote mitochondrial dysfunction and inflammation in ischemic acute kidney injury by disrupting TFAM-mediated mtDNA maintenance. Theranostics. 2021;11(4):1845–63.
42. Rajendrakumar SK, Revuri V, Samidurai M, Mohapatra A, Lee JH, Ganesan P, Jo J, Lee YK, Park IK. Peroxidase-mimicking nanoassembly mitigates lipopolysaccharide-induced endotoxemia and cognitive damage in the brain by impeding inflammatory signaling in macrophages. Nano Lett. 2018;18(10):6417–26.
43. Natoli G, Chiocca S, Nuclear Ubiquitin Ligases. NF-κB degradation, and the control of inflammation. Sci Signal. 2008;1(1):pe1.
44. Sun SC. The non-canonical NF-κB pathway in immunity and inflammation. Nat Rev Immunol. 2017;17(9):545–58.
45. Ou QM, Tan LP, Shao YT, Lei FC, Huang WY, Yang N, Qu Y, Cao ZY, Niu LH, Liu Y, et al. Electrostatic charge-mediated apoptotic vesicle biodistribution attenuates sepsis by switching neutrophil NETosis to apoptosis. Small. 2022;18(20):2200306.
46. Soni M, Handa M, Singh KK, Shukla R. Recent nanoengineered diagnostic and therapeutic advancements in management of Sepsis. J Controlled Release. 2022;352:931–45.
47. Kumar V. Pulmonary innate immune response determines the outcome of inflammation during pneumonia and sepsis-associated acute cclung ccinjury. Front Immunol. 2020;11:1722.
48. Xu CC, Zhang L, Xu SY, Wang ZC, Han Q, Lv Y, Wang XF, Zhang XX, Zhang QJ, Zhang Y, et al. Neutrophil ALDH2 is a new therapeutic target for the effective treatment of sepsis-induced ARDS. Cell Mol Immunol. 2024;21(5):510.
49. Manickam C, Shah SV, Lucar O, Ram DR, Reeves RK. Cytokine-mediated tissue injury in non-human primate models of viral infections. Front Immunol. 2018;9:2862.

50. Hotchkiss RS, Monneret G, Payen D. Sepsis-induced immunosuppression: from cellular dysfunctions to immunotherapy. Nat Rev Immunol. 2013;13(12):862–74.

Publisher's note